Ocean stratification impedes particulate transport to the plumes of Enceladus

communications earth & environment

Article

https://doi.org/10.1038/s43247-025-02036-3

Ocean stratification impedes particulate transport to the plumes of Enceladus

Flynn Ames [1] ✉, David Ferreira [1], Arnaud Czaja[2] & Adam Masters[2]

Water-vapour plumes erupting from Enceladus' south pole provide a window into the properties of its subsurface ocean, a prime target in the search for life. However, the extent to which plume material represents conditions at Enceladus' depths is unclear, because of its unknown ocean stratification, which may impede the transport of matter to the ocean top. Previous studies have found conflicting stratification regimes using differing parameter choices and model physics. Here, we build a comprehensive view of Enceladus' ocean stratification and bottom-to-top transport timescale, across plausible ranges of salinity and tidally- and librationally-induced mixing, accounting for non-linearities in the equation of state for water, geothermal heating and ice-ocean freshwater exchanges. We use theoretical models verified with global ocean numerical simulations. We show that, under a steady state assumption for the ice shell, which requires melting at the poles, there is no parameter choice permitting an unstratified ocean from top to bottom there. As a result, potential hydrothermal products take at minimum 100s of years to reach the plumes. This suggests that either timescales of several months, inferred from Cassini observations, are incorrect, perhaps biased by alternative particulate transport mechanisms, or that Enceladus' ice shell is not in a quasi-equilibrated state.

Global oceans of liquid water underlay the surface of several icy satellites in our solar system and among them Enceladus—a ~500 km wide moon of Saturn—is a leading astrobiological target[1–5]. Unique to Enceladus are the geyser-like plumes containing water vapour and ice grains that erupt continuously from fissures in its south polar ice shell[6]. These plumes, sustained by tidal stresses imparted by Enceladus' eccentric orbit about Saturn[7,8], eject ocean material into space, providing an opportunity to probe its composition.

Existing interpretations of plume vapour and particulates, sampled via the Cassini spacecraft, hint at an ocean conducive for life[9], with possible submarine hydrothermal activity at the ocean bottom[10,11], perhaps fuelled by tidal heating in Enceladus' rocky core[12]. Combined with detected CHNOP bio-essential elements[13,14], and low ocean pressures (owing to Enceladus' weak gravity), this implies physico-chemical environments at depth comparable to those around submarine hydrothermal vent fields on Earth, which provide the redox agents necessary for chemosynthetic life[15–17].

Given the recent prioritisation of a mission returning to Enceladus, dedicated to probing plume material as a means to constrain Enceladus' biogeochemistry and search for evidence of extant life[18], it is necessary to estimate the extent to which plume material (sourced from a localised region near Enceladus' south polar ocean-ice interface) can be assumed representative of the ocean bottom, where hydrothermal systems capable of supporting life may exist. Previous work highlighted fractionation processes within the geyser conduit as a means to create compositional differences between the plume and ocean [e.g.,[19]]. Here we highlight the role of ocean stratification (measuring the strength of density layering within the ocean), which if present, could isolate the ocean-ice interface from the ocean bottom and yield plume material that misses components present at depth.

Stable stratification inhibits convection—an efficient mechanism for vertical transport of particulates and dissolved substances[20]. In Earth's predominantly stably stratified ocean[21] this permits the marine snow phenomena, where organic matter, unable to maintain neutral buoyancy, undergoes 'detrainment', settling down to the ocean bottom[22–24]. Meanwhile, the slow ascent of hydrothermally derived, dissolved substances provides time for scavenging processes and usage by life, resulting in surface concentrations far lower than those present nearer source regions at depth[25–29].

In contrast, Enceladus' ocean has been assumed in much previous work to be convecting from top to bottom (thus entirely unstratified—Fig. 1, upper left), able to efficiently transport hydrothermally derived substances to the plumes[10,12,20]. The assumption is made on the basis that Enceladus' ocean is cooled from above and heated from below, by an ice shell (via conductive or convective heat loss) and tidally heated rocky core,

[1]Department of Meteorology, University of Reading, Reading, RG6 6ET, UK. [2]Department of Physics, Imperial College London, London, SW7 2BW, UK.
✉e-mail: f.ames@pgr.reading.ac.uk

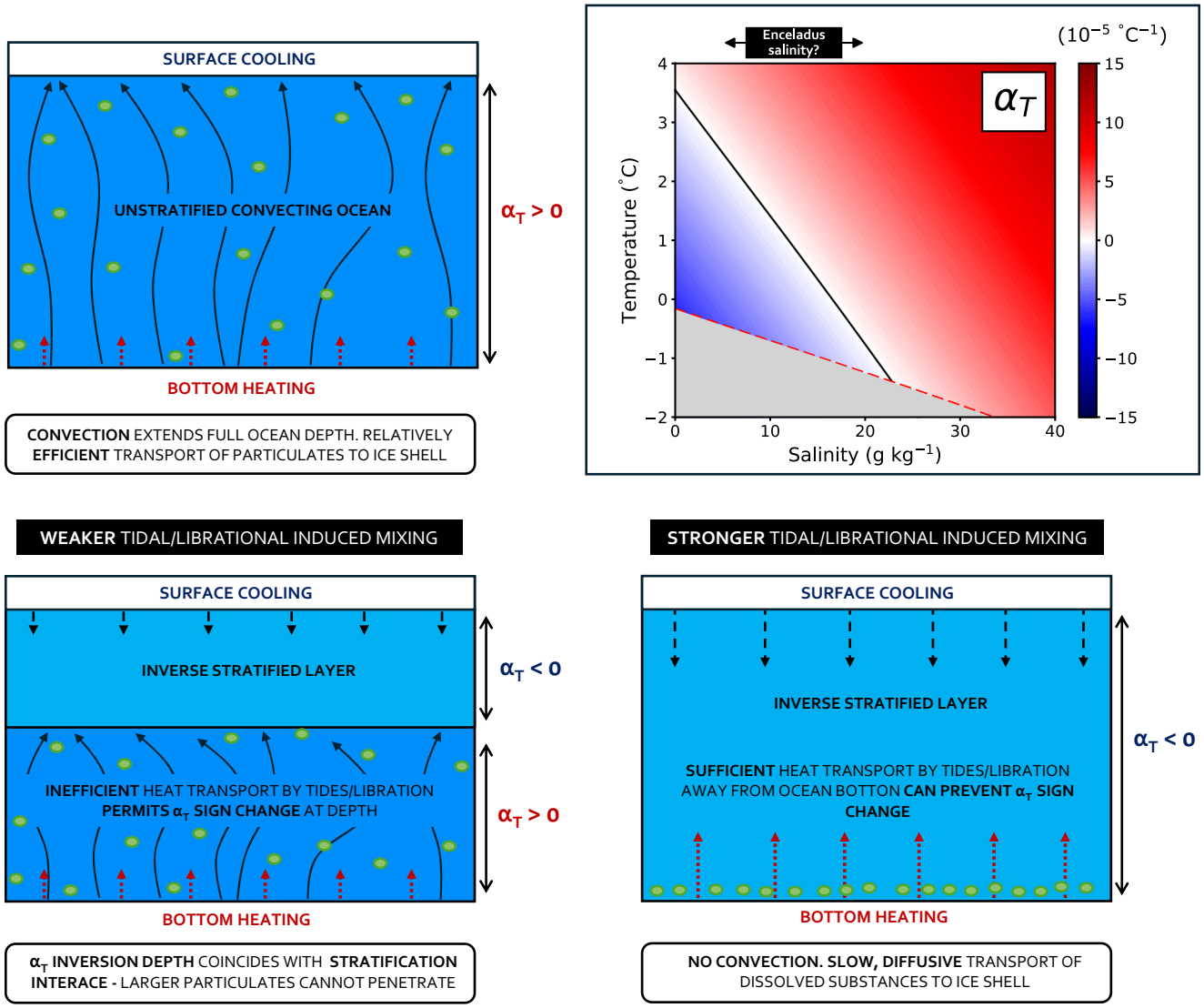

Fig. 1 | Inverse Stratification and particulate transport within Enceladus' ocean. **Upper right**: Thermal expansion coefficient (α_T - °C^{-1}) plotted as a function of temperature (°C) and salinity (g kg^{-1}) at constant pressure, computed under 20 km mean ice thickness for Enceladus. Black line denotes where α_T changes sign. Black box with arrows denotes the range of uncertainty for Enceladus' mean ocean salinity (5-20 g kg^{-1}) implied by Cassini E-ring ice grain observations[30]. Red dashed line denotes the water freezing temperature (corresponding to the temperature at ice interface), using the formulation of[55]. Grey shading denotes frozen water. Water density is computed using the non-linear equation of state of ref. 52. **Schematics**: Illustrating an idealised ocean beneath Enceladus' south polar ice shell, either entirely unstratified (and thus convecting; **upper left**) or inversely stratified owing to negative α_T (**lower left** and **lower right**). Where $\alpha_T < 0$, cooling from the overlying ice makes water more buoyant, while warming from the underlying core makes water denser. These effects reverse where $\alpha_T > 0$, and the resultant presence of buoyant water underlying denser water induces convective overturning (indicated with solid black arrows). Dashed arrows denote the magnitude of assumed tidally and librationally induced mixing, parameterised in this work as κ_z. Red dotted lines denote heat transport by induced mixing, achieved for the same bottom heat flux. Green circles denote hypothetical particulates unable to attain neutral buoyancy where the ocean is stably stratified (light blue shading), but entrained where the ocean convects (dark blue shading). Note these schematics assume no other mechanisms for stratification of Enceladus' ocean.

respectively. However, such boundary forcings can only induce convection where the thermal expansion coefficient (α_T—quantifying the expansion of water with increasing temperature) is positive, so that colder water is denser and thus sinks. For water of salinity $\lesssim 20$ g kg^{-1} (Enceladus' ocean salinity as implied by Cassini ice grain observations [30]), α_T is in fact negative near its freezing point (which is necessarily approached at the ocean-ice interface) (Fig. 1, upper right). This means that cooling from above, rather than inducing convection, should act to increase water buoyancy and promote the development of a stratified layer underlaying the ice shell[31]. The same mechanism for stratification occurs in freshwater lakes on Earth during winter and is commonly referred to as inverse stratification[32,33], terminology that will be used here.

An inverse stratification was previously suggested for Europa by[34] but as pointed out by[31], is more likely for Enceladus due to its lower pressures (compared to Europa), which could permit negative α_T (and thus inverse stratification) to extend the full ocean depth[35]. Increasing temperature can also force α_T to become positive (Fig. 1, upper right). This could allow bottom heating to maintain a positive α_T at depth provided sufficient heat can accumulate there. Heat accumulation would be controlled in part by the magnitude of the bottom heat flux, but also by processes that can move colder waters from the ice-interface downwards, and heat away from the ocean bottom, in the absence of convection. These processes would include molecular diffusion, but could be made far more efficient within Enceladus by mixing induced by tides and ice shell libration (periodic movement of the ice shell over the ocean;[36]). If induced mixing is strong enough to ensure a negative α_T at all depths, Enceladus' ocean could be entirely stably stratified (Fig. 1, lower right). If induced mixing is weak, an inverse stratified layer would instead overlay

a well-mixed convecting layer, separated by the depth at which α_T becomes negative (Fig. 1, lower left), henceforth referred to as the inversion depth.

The existence or extent of inverse stratification within Enceladus is currently poorly constrained. Only a handful of simulations have been conducted at salinity ≤ 20 g kg^{-1}, computing water density using a non-linear equation of state that permits a varying α_T (thus permitting an inversion depth). These include a localised (albeit unequilibrated) simulation by[37] which produced an entirely inversely stratified ocean beneath the Enceladus' south pole (akin to Fig. 1, lower left), along with two localised simulations by[38], one of which produced an inversion depth ~ 30 km beneath the surface (akin to Fig. 1, lower right). Equilibrated global simulations of Enceladus' ocean were conducted at 8.5 g kg^{-1} salinity by both[31] and[39], with an inversion depth obtained in both simulations. However, as in the aforementioned studies[31,39], tested only one value of κ_z—an effective vertical diffusivity used to parameterise the vertical mixing induced by tides and libration[36]. By approximating κ_z as a function of the total energy available for ocean mixing, ref. 31 derived the range of uncertainty of κ_z within Enceladus to span five orders of magnitude, from ~10^{-7} to 10^{-3} m^2 s^{-1}, corresponding to existing bounds in estimates of tidal and librational energy dissipation[40,41]. The sensitivity of ocean stratification within Enceladus to κ_z, and implications for the transport of hydrothermally derived particulates and dissolved substances to the ice shell, has not yet been explored.

Inferences from Cassini observations of silica nano-particles—believed to be sourced from hydrothermal alteration within Enceladus' core—suggest transport timescales through Enceladus' ocean of several months[10]. However, it is important to test how this fits within constraints provided by fluid dynamics and whether inferred transport timescales could be achieved within the plausible parameter space in ocean salinity (determined by[10] as not exceeding ~40 g kg^{-1}) and κ_z. With this in mind, the geometry of the overlying ice shell could provide additional constraints upon ocean stratification that should be accounted for[42,43]. Enceladus' ice shell appears to be thicker at the equator than at the poles[44]. To maintain a steady state ice thickness, melting would be required at the poles and freezing at the equator, to balance the expected poleward ice flow[45–47]. Stratified polar freshwater melt has previously been shown to provide a barrier to vertical particulate transport in high-resolution, localised simulations[38], although these were not run to equilibrium.

The novelty of this manuscript is a comprehensive investigation of ocean stratification within Enceladus across the plausible parameter space in ocean salinity and κ_z, and the explicit computation of the transport timescales of entrained particulates and dissolved substances (hereafter 'tracers') from source regions at depth, to the south polar plumes. We first build upon previous work[31] to develop a simple theoretical model specific to inverse stratification and corresponding tracer transport timescales. We then perform numerical simulations using an ocean general circulation model to verify the theory while accounting for ice shell melting and freezing, under the assumption of steady state. Finally, we discuss the implications of our results for interpretations of plume material and the state of Enceladus' ice shell.

Theoretical model

Inverse layer thickness

Following common practice in Earth ocean modelling, tidally and librationally induced mixing is parameterised using an effective vertical diffusivity κ_z. In Earth's oceans, a complex pathway links tidal energy dissipation to its mixing effects, involving the emission, transmission, and breaking of internal waves[48]. However, κ_z has proved to be a good first order representation of this pathway in ocean models[49]. As on Earth, κ_z may exhibit spatial and temporal variations within Enceladus due to stratification, topography, and profiles of tidal and librational energy dissipation, which may be concentrated within boundary layers at the ocean top and bottom[50]. Given existing uncertainties, κ_z here is assumed constant and uniform.

By assuming κ_z dominates vertical heat transport in the inverse stratified layer, a steady state heat balance requires that the vertical diffusive flux is equal to the geothermal heat flux at any depth in the inverse layer:

$$Q = c_p \rho_0 \kappa_z \frac{\partial T}{\partial z}, \tag{1}$$

where Q is the geothermal heat flux (W m^{-2}), c_p the specific heat capacity (J kg^{-1} K^{-1}) and ρ_0 the ocean density (kg m^{-3}).

The top of an inverse layer, in contact with the ice-ocean interface, is at freezing point T_f, while the bottom of this layer, the inversion depth, is at the critical temperature T_{crit}—the temperature at which α_T changes sign for a given salinity and pressure (solid black line in Fig. 1, upper right). Integrating across the inverse layer gives[31]:

$$H_{strat} = D(T_{crit} - T_f), \tag{2}$$

where $D = \frac{c_p \rho_0 \kappa_z}{Q}$, and H_{strat} is the thickness of the inverse layer. Note that for inverse stratification, which requires $\alpha_T < 0$, to exist, T_{crit} must be higher than T_f (ocean temperature cannot fall below freezing point—see Fig. 1, upper right).

T_{crit} varies with pressure, and is therefore not independent of H_{strat}. To make analytical progress, T_{crit} is approximated as a linear function of salinity and pressure:

$$T_{crit} \approx aS + bP + c, \tag{3}$$

where we find, a = −0.216 °C (g kg^{-1})$^{-1}$, b = −2.11 x 10^{-7} °C Pa^{-1}, and c = 4.01 °C, across the range of salinity and pressure plausible for Enceladus (see Methods, section: Critical Temperature Computation and Fitting).

Ocean pressure can be approximated as $P = P_{int} + P_{ocn}$, the pressure at the ice-ocean interface and pressure contribution from any overlying ocean respectively. $P_{int} = \rho_i g H_i$, where g denotes gravity (m s^{-2}) and H_i and ρ_i denotes ice thickness (m) and density (kg m^{-3}). Using the hydrostatic approximation, at the inversion depth:

$$P_{ocn} = \rho_0 g H_{strat}. \tag{4}$$

Substituting Eqs. (3) and (4) into Eq. (2), an approximation for the inverse layer thickness can be obtained:

$$H_{strat} = \frac{D(T_{crit*} - T_f)}{1 - Dbg\rho_0}, \tag{5}$$

where $T_{crit*} = aS + bP_{int} + c$ is the critical temperature evaluated at the ice-ocean interface, and is independent of H_{strat}. To the first order, Eq. (5) has the same physical interpretation as proposed by[31]: Increasing bottom heat flux Q increases the thickness of the bottom convective layer, reducing the inverse layer thickness H_{strat}, while a larger vertical diffusivity κ_z is more effective at transporting the geothermal flux upward, thus reducing the penetration of convection and increasing the inverse layer thickness. Compared to[31] however, Eq. (5) shows a non-linear dependence on Q and κ_z owing to the additional $\frac{1}{1-Dbg\rho_0}$ factor derived here. Eq. (5) also explicitly includes a salinity dependence through T_{crit*} (note that T_f also depends on S and P_{int}, but the behaviour of $T_{crit*} - T_f$ is dominated by that of T_{crit*}; see Methods). Further interpretation of Eq. (5) is discussed below.

Tracer age

The transport timescale of tracers sourced from the ocean bottom to the south polar plumes, gives a lower bound residence time for such tracers in Enceladus' ocean (i.e., before ejection into space)—this timescale will henceforth be referred to as the tracer age. Assuming the transport timescale through any underlying convecting layer is negligible, the time taken to

traverse diffusively through an inverse stratified layer of thickness H_{strat}, given a mixing κ_z is:

$$\tau = \frac{H_{\mathrm{strat}}^2}{2\kappa_z}. \quad (6)$$

Note that tracer age τ is not inversely proportional to κ_z because H_{strat} is itself a function of κ_z.

It is worth emphasising that our timescales do not account for detrainment of matter, which could further prolong transport timescales, and even prevent sufficiently large, dense or compacted particulate matter—unable to attain neutral buoyancy—from ever being transported to the plumes[20]. Because of this, and the neglect of the time in the convective layer and transit time within the ice shell, tracer ages derived here should be interpreted as lower bounds on the transport timescale from the ocean's bottom to the plumes.

Analytical solutions across plausible range of salinity and κ_z

Solutions for the inverse layer thickness and tracer age from Eqs. (5) and (6) are shown in Fig. 2 (left). These are computed across the plausible range of ocean mean salinity and κ_z for Enceladus. Bottom heating Q is set to 0.03 W m^{-2}, the approximate globally averaged heat flux at the inversion depth, assuming a total core heat output of 20 GW, in the middle of the 10-30 GW range proposed by[12]. Interface pressure is computed assuming a mean ice thickness of 20 km, mean ice density of 925 kg m^{-3}, and gravity of 0.113 m s^{-2}.

The predicted tracer age varies by over six orders of magnitude depending upon the chosen values of mean salinity and κ_z, with an inverse layer thickness ranging from metres to the entire ocean depth.

For a given κ_z, lower salinity is predicted to yield a thicker inverse layer. This is because T_{crit} (see Eq. (3)) is warmer at lower salinity, and can be attained (allowing the inverse layer to extend) closer to the heat source at the bottom. A larger inverse layer thickness, in turn, results in older tracers in the plumes, owing to the greater distance that must be traversed diffusively. The dependence of H_{strat} on the mean salinity is linear through $(T_{\mathrm{crit}*} - T_{\mathrm{f}})$ (see Eq. (5)), except if H_{strat} reaches the full ocean depth (Fig. 2, top left).

For a fixed salinity, a larger κ_z results in a thicker inverse layer. The behaviour is complex due to the non-linear dependence of H_{strat} on κ_z (Eq. (5)) and saturation upon H_{strat} reaching the ocean depth (set to 40 km here). At high salinities, $T_{\mathrm{crit}*}$ is much nearer the freezing temperature (Fig. 1, upper right) (or equally, ocean pressures are more likely to force α_T to become positive at depth). As a result, beyond ~20 g kg^{-1}, the inverse layer is shallow and weakly sensitive to κ_z. Conversely, at low salinities where the $T_{\mathrm{crit}*} - T_{\mathrm{f}}$ difference is large, H_{strat} is highly sensitive to κ_z. While H_{strat} increases linearly with κ_z for low κ_z, the aforementioned non-linear effect kicks in quickly and H_{strat} increases slowly with κ_z at higher κ_z. This is because the increase in H_{strat} that results from increasing κ_z causes T_{crit} to become cooler through its pressure dependence, counteracting the ability of

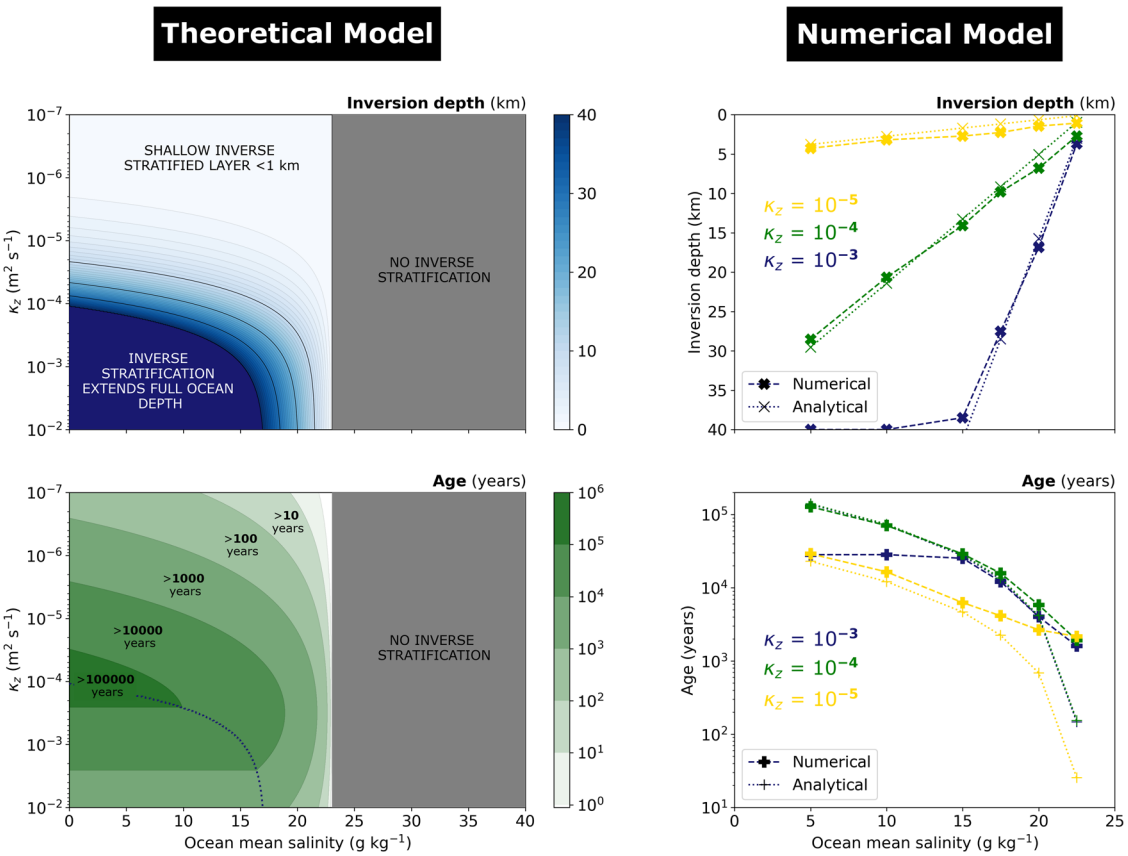

Fig. 2 | Stratification and tracer age—results. Top Left: Inversion depth H_{strat} (km—depth at which thermal expansion coefficient α_T becomes negative, taken here to define the inverse stratified layer thickness) computed using Eq. (5), plotted as a function of ocean mean salinity (g kg^{-1}) and vertical diffusivity κ_z (m^2 s^{-1}) plausible for Enceladus. Contours denote 1 km (and black contours 10 km) depth up to the assumed 40 km ocean depth for Enceladus, shaded in midnight blue. Grey shading denotes where inverse stratification cannot occur, because α_T cannot become negative at the ocean-ice interface pressure (computed under the 20 km mean ice thickness for Enceladus). **Bottom Left**: Tracer age (years) at the ocean-ice interface, computed using Eq. (6). Note that age contours are logarithmic. Blue dotted line delineates parameter space where inverse stratification is predicted to extend the full ocean depth. Within this parameter space, age contours are horizontal, with no predicted salinity dependence. **Top right**: Numerical solution for the inversion depth (thick cross, dashed line) across a range of ocean mean salinity for three values of κ_z, denoted with different colours. This is plotted alongside the analytical solution (thin cross, dotted line) for comparison. Where the inversion depth equals the ocean depth, the whole ocean is inversely stratified. **Bottom right**: Numerical solution for the ideal age at the south polar ocean-ice interface (thick plus, dashed line), plotted alongside the analytical solution (thin plus, dotted line) for comparison. Note that age does not fall below 1000 years in any numerical simulation.

the inverse layer to expand downward. At fixed salinity, the maximum value of H_{strat} ($=(T_{crit*} - T_f)/(-bg\rho_0)$) is approached for large mixing. For our parameter choices, this maximum value ranges from ~160 km at S=0 g kg^{-1} to ~20 km at 20 g kg^{-1}. Importantly, beyond about 17 g kg^{-1}, the maximum inverse layer thickness is less than the ocean depth, i.e., limited by properties other than the ocean geometry.

Turning to the tracer age (Fig. 2, bottom), for low κ_z ($\leq 10^{-4}$ m^2 s^{-1}), the tracer age increases with the inverse layer thickness (thicker layers take longer to traverse). For larger κ_z, where the inverse layer saturates at either the ocean depth or its maximum H_{strat}, further increasing κ_z makes transport through the inverse layer more efficient, decreasing tracer age. As a result, the maximum ages are obtained at $\kappa_z \approx 10^{-4}$ m^2 s^{-1}, i.e. the lowest κ_z for which the inverse layer extends the ocean depth. Despite this, an inverse layer of 50 m can still produce ages exceeding 100 years at the lowest κ_z tested, because transport is inefficient in this case.

Note that Eqs. (5) and (6) can be applied to any moon, planet or dwarf planet containing an ocean heated from below and permanently overlain by ice (see Methods, section Application to Other Icy Moons for application to Europa).

Tests with a numerical global ocean circulation model

Our 1D theoretical model neglects lateral gradients in ocean salinity (driven by ice shell melting and freezing), and in temperature (owing to the pressure dependence of freezing temperature) that could drive an overturning circulation in Enceladus' ocean. The associated heat transport could challenge the assumption of Eq. (5), that vertical heat transport in the inverse stratified layer is dominated by κ_z. We therefore test the robustness of our 1D theoretical model against a non-linear 2D global ocean model.

Model description

We use the Massachusetts Institute of Technology Ocean General Circulation Model (MITgcm;[51]) in a 2D latitude-depth setup configured for Enceladus. A fully non-linear equation of state is employed[52], with water density computed (and α_T allowed to vary) as a function of ocean pressure, salinity and temperature. Freshwater fluxes from the ice shell are prescribed, under the assumption of steady state[53], by computing the ice shell melting and freezing necessary to balance the ice flow induced by an idealised poleward-thinning ice shell geometry[47,54]. This results in freshwater input (ice melting) at the poles and freshwater output (ice freezing) at the equator, as previously proposed[45]. Temperature is restored to the pressure-dependant freezing point at the ocean top, computed using the same idealised geometry[55], yielding polar ice-interface temperatures ~ 0.1 °C warmer than at the equator (see Fig. S1). The upper boundary in the model simulation is flat for simplicity. A polar amplified geothermal heat flux is applied at the ocean bottom assuming a total core output of 20 GW[12]. Unresolved mixing by convection is parameterised via the diffusive adjustment scheme of ref. 56. Ocean mesoscale eddies are parameterised using the Gent-McWilliams and Redi schemes[57,58]—a standard combination in Earth ocean modelling, but modified here for icy moon oceanography (see Methods).

Borrowing from studies of ocean ventilation on Earth [e.g.,[59]], solutions for tracer age are obtained by computing the ideal age. This defines the (volume-weighted) time elapsed since a water parcel lost contact with the ocean bottom. As for the theoretical age (section: Tracer Age), the numerical age is a lower bound on the transport timescale of tracers from the ocean bottom to the south polar plumes.

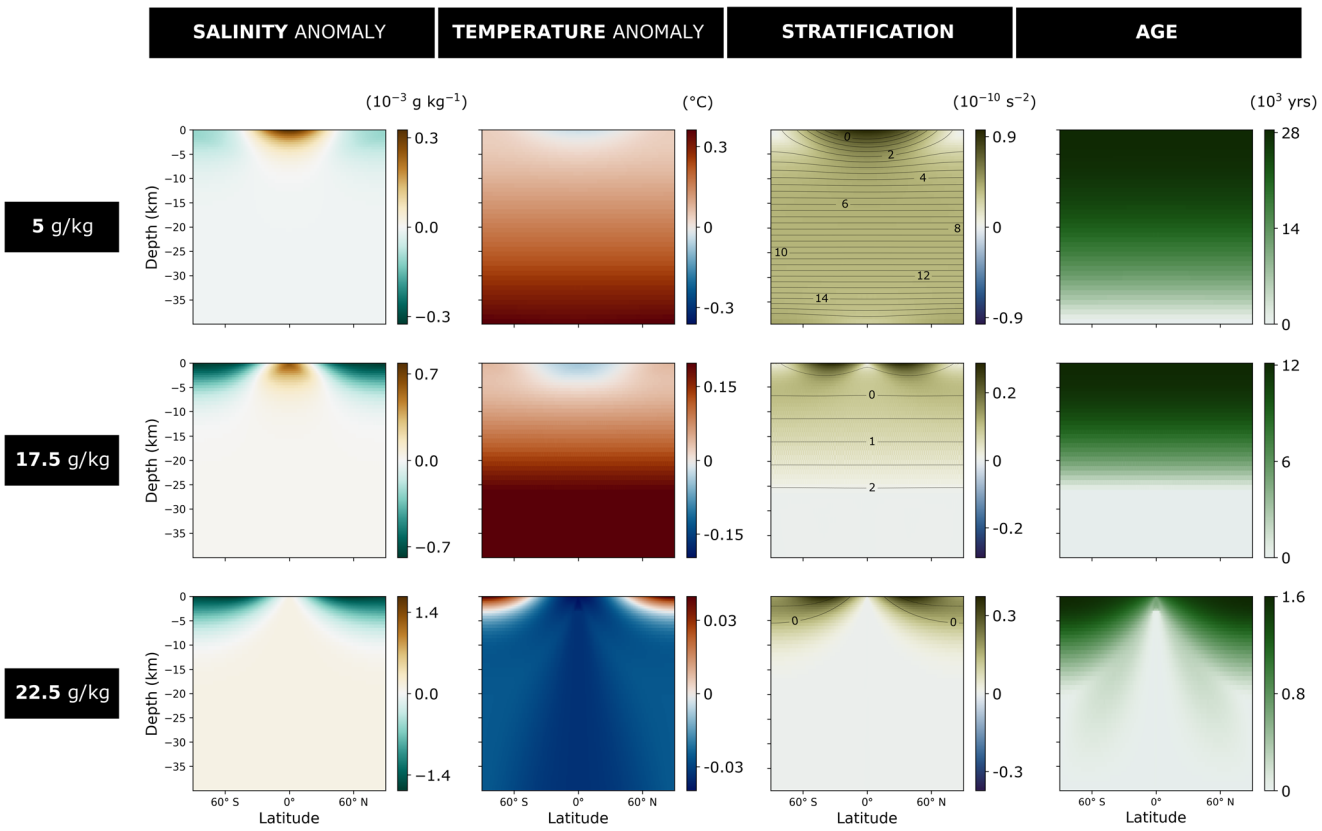

Fig. 3 | Temperature, salinity, stratification and age—2D fields. Numerical solutions with effective vertical diffusivity $\kappa_z = 10^{-3}$ m^2 s^{-1}, across three different mean ocean salinities of 5 (top), 17.5 (middle), and 22.5 (bottom) g kg^{-1}, highlighting three contrasting stratification regimes. Note colour bar scales are saturated and vary throughout. **First column**: Salinity anomaly (g kg^{-1}) taken about the mean salinity. **Second column**: Potential temperature anomaly (°C) taken about the simulation reference temperature T_{ref} (freezing temperature computed under 20km mean ice thickness) of -0.433 (top), -1.106 (middle) and -1.379 (bottom) °C. **Third column**: Shading shows the buoyancy frequency N^2 (s^{-2}) indicating stratification. Contours show the potential density anomaly (10^{-3} kg m^{-3}) about the ocean reference density ρ_0 of 1008.984 (top), 1015.029 (middle) and 1019.065 (bottom) kg m^{-3}. Potential density here is computed using the reference pressure P_{ref} evaluated at the ocean-ice interface. **Fourth column**: Ideal age of tracers (years), sourced from the ocean bottom.

Simulations are performed across a range of plausible ocean mean salinity (5, 10, 15, 17.5, 20, 22.5 g kg^{-1}), and κ_z (10^{-3}, 10^{-4}, 10^{-5} m^2 s^{-1}). Extended model details can be found in the section Model Configuration Details.

Numerical solutions

Numerical solutions for the globally averaged inversion depth, along with the tracer age at the south polar ice interface, are plotted in the right panel of Fig. 2. Analytical solutions using Eqs. (5) and (6), are plotted alongside for comparison. Corresponding 2D fields of ocean temperature, salinity, stratification, and ideal age are shown in Fig. 3. The inversion depth is chosen as a metric for the thickness of the inverse layer. An alternative metric, the depth at which convection extending from the ocean bottom ceases, gives nearly identical results (see Fig. S2).

Numerical and analytical solutions for the inversion depth show good agreement. Two solutions ($\kappa_z = 10^{-3}$ m^2 s^{-1} and salinity ≤ 10 g kg^{-1}) exhibit a stratified inverse layer extending through the entire ocean depth (no convection).

In all other solutions with salinity ≤ 20 g kg^{-1}, an interface develops at the inversion depth, between a cooler inverse stratified layer underlying the ice shell, and a warmer convecting layer underneath (Fig. 3, middle). In the convective layer, the temperature is nearly homogeneous at $\approx T_{\mathrm{crit}}$, owing to efficient mixing there, as found previously[39]. A lateral temperature gradient develops at the ice-ocean interface in all solutions owing to the pressure-dependant freezing temperature there, warmer at the poles, cooler at the equator. In the 5 g kg^{-1} solution, this results in enhanced stratification at the equator relative to the poles at the highest κ_z tested (Fig. 3, upper). Similarly, salinity gradients develop at the ice interface in response to the imposed melting and freezing forcing pattern (see Fig. S1). Despite these, the horizontally averaged inversion depth follows closely the 1D theoretical model discussed in the section Analytical Solutions Across Plausible Range of Salinity and κ_z.

Numerical and analytical solutions for the tracer age in general show good agreement, but with larger relative discrepancies where salinity $\gtrapprox$ 20 g kg^{-1} (Fig. 2, bottom right). Discrepancies tend to be larger at the lowest κ_z tested, because the inversion depth is shallow in this case, meaning this and the corresponding age are more sensitive to the employed vertical resolution (~300 m at the ocean-ice interface, see Methods). However discrepancies are pronounced at 22.5 g kg^{-1}, where numerical solutions for tracer age converge to ~1000 years across all κ_z tested, and the inverse stratification theory appears to break down. This can be explained by the effects of ice shell melting and freezing, which are not captured by the 1D theoretical model. Freshwater melt at the pole (necessary to maintain Enceladus' ice geometry assuming steady state) induces salinity anomalies that become the dominant control upon ocean density for salinity $\gtrapprox$ 10 g kg^{-1} (owing to weaker α_T nearer the ice interface, see Fig. 1), resulting in stably stratified, buoyant, freshwater lenses at both poles. For salinity > 20 g kg^{-1}, the freshwater lens penetrates deeper than the inversion depth becoming the dominant control upon the transport timescales of tracers to the polar ice shell.

At the equator, saltier water (generated by ice freezing) can penetrate the inversion depth in solutions with 22.5 g kg^{-1} mean salinity. There, convection exists much closer to the ice-interface than at the poles. Despite this, age is still of order 100's of years at equatorial ocean top (see also numerical solution at lower κ_z in Fig. S3). This is because a weak stratification is maintained here against convection by the eddy parameterisation scheme (see Methods). The eddy scheme is invoked because ice melting and freezing induce lateral gradients in ocean density, causing isopycnals (contours of constant density—see Fig. 3, middle right panel) to become 'sloped'. As in Earth's oceans, the parameterised eddies mimic the effect of baroclinic instability which extracts the potential energy stored in the sloped isopycnals and, in doing so, flattens them, re-stratifying the water column [see also[43,60]].

Also note the stratifying influence of eddies is likely modulated by the shape of the overlying ice shell—an effect not considered here. Because Enceladus' ice shell is expected to extend deeper into the ocean at the equator than at the poles, freezing should occur lower down in the water column than melting. Where salinity anomalies are the dominant control upon ocean density (e.g., Fig. 3, lower), a large κ_z would be necessary to mix the buoyant (fresher) water downwards to sustain the lateral density gradient at the equatorial ice interface[36]. Without this, equatorial eddy restratification would likely be weaker than obtained in our numerical solutions for this regime. Numerical solutions for the equatorial age should be interpreted with this in mind.

To quantify the potential control of freshwater melt upon tracer age at the south pole, we use the scaling proposed by[60] for the thickness of a freshwater lens:

$$H_{\mathrm{lens}} \sim R\sqrt{\frac{\kappa_z}{\kappa_{\mathrm{GM}}}}, \tag{7}$$

where κ_{GM} is the eddy diffusivity and R a horizontal length scale defining the horizontal scale of salinity contours within the freshwater lens (which closely follows a region of melting—see Fig. 3 and Fig. S1), taken here to equal the moons radius ($\sim \frac{1}{3}$ the length of the simulation domain). As noted by[61] and[60], this scaling is applicable only where these salinity contours do not intersect the ocean bottom.

Where H_{lens} is deeper than the inversion depth, we can substitute Eq. (7) into Eq. (6) to obtain an estimate for the tracer age at the south polar ice shell:

$$\tau \sim \frac{R^2}{2\kappa_{\mathrm{GM}}}. \tag{8}$$

Note the cancellation of κ_z here: lower κ_z results in a thinner freshwater lens to be traversed, but this effect is offset because lower κ_z also yields less efficient vertical transport through this layer. Substituting in $\kappa_{\mathrm{GM}} = 1$ m^2 s^{-1} from the numerical model setup (see Methods), Eq. (8) yields a tracer age τ ~ 1000 years, in approximate agreement with the numerical solutions (Fig. 2, bottom right). Additional tests suggests that at very low κ_{GM} (0.01 m^2 s^{-1}) the steepening of isopycnals in a freshwater lens (owing to a deeper penetration into the ocean interior in accordance with Eq. (7)) allows along-isopycnal transport by eddies to become an increasingly significant contributor to the vertical tracer transport. This, combined with the saturation of H_{lens} at the ocean depth, increases discrepancies relative to Eq. (8). Yet, because κ_{GM} is weak in this instance, the tracer age remains larger than 10,000 years (see Fig. S4).

Discussion

In this work, we investigate ocean stratification within Enceladus' ocean and implications for the transport of hydrothermally derived particulates and chemical species (tracers) to the south polar plumes. We develop analytical expressions for the stratification and corresponding tracer bottom-to-top transport timescales and test these successfully using a global ocean general circulation model. We explore a range of plausible salinity and tidally and librationally induced mixing κ_z, accounting for the non-linearities in the equation of state for water, geothermal heating and freshwater exchanges at the ocean-ice interface.

A key outcome of our study is that, regardless of the values of the salinity and mixing κ_z, there always exists ocean stratification that impedes transport to the south polar ice-interface. Ocean stratification within Enceladus is controlled to the first order by its ocean salinity, in combination with non-linearities in the equation of state for water density. Schematically, there are two limits:

- In the low salinity limit, permitting a negative α_T, cooling from the overlying ice shell stratifies the underlying ocean, as occurs in cold freshwater lakes on Earth (referred to as inverse stratification). Existing uncertainty in induced mixing yields stratification that could extend anywhere from 10's of metres to 10's of kilometres beneath the ice-interface (Fig. 2, upper left).
- At high salinities, enough to prevent α_T becoming negative, polar freshwater melt—required under the assumption of steady state—

ensures the upper ocean remains stably stratified by freshwater lenses overlying a well-mixed ocean.

Crucially, the thinnest inverse layers and freshwater lenses are reached for low mixing rates, which are also inefficient at transporting tracers. As a result, transport timescales to the plumes do not fall below 100's of years (see Eqs. (1) and (8)). At the other end of the range, transport timescales could possibly exceed 100000 years (Fig. 2). In any case, such timescales provide opportunity for alteration between synthesis at depth and ejection out to space.

Our estimates are inconsistent with the inferences of several months made from Cassini observations of size-fractionated silica nanoparticles in Saturn's E-ring[10]. This discrepancy could possibly be explained by alternative particulate transport processes not considered here. For example, mechanisms associated with the opening of the plume conduit could perhaps pull nano-particles up from underneath a stratified layer. Hydrogen gas bubbles have been suggested as an alternative nano-particle transport mechanism, but only when assuming an unstratified ocean[62]. It has also been suggested that size-fractionated silica nanoparticles could be produced by non-hydrothermal processes[63], for example, photolytic decomposition of silica-saturated ice grains after ascent through the geyser conduit[64]. If the source of observed nano-particles is not Enceladus' core, Cassini observations are not necessarily inconsistent with ocean stratification at Enceladus' south pole.

Alternatively, the discrepancy may suggest that our assumption of a steady state ice shell is incorrect. This assumption implies ice melting at the poles that maintains a stratification there and, as a result, large transport timescales, even in an otherwise predominantly convecting ocean. If Enceladus' ice shell is freezing at the poles, this could be sufficient to break down ocean stratification beneath the plumes. This would require that Enceladus' ice shell is not in a quasi-equilibrated state, which has been proposed owing to the inability of tidal heating models to reproduce the heating necessary to balance the observed heat outflow from Enceladus' south polar ice shell[65,66]. These issues are currently being debated [see[12,38,47,67]] and go beyond the scope of the present work.

Our work approaches the problem from a fluid dynamics perspective, complimentary to direct numerical simulations that can resolve much finer scale ocean dynamics [e.g.,[68,69]], but currently not the effects of ocean salinity and non-linearity in the equation of state for water density.

Our results emphasise that a robust evaluation of the stratification must use a non-linear equation of state that accounts for variation of the thermal expansion coefficient with temperature, salinity and pressure as well as account for the ice-ocean freshwater exchanges that create salinity gradients. We find that, under a steady state assumption and under observed constraints on geothermal heating and the shape of Enceladus' ice shell, there is no regime with bottom-to-top convection underneath the plumes. Future studies should make careful use of the assumption of a well-mixed ocean on Enceladus (and other icy moons).

We end in noting that stratification interfaces within Enceladus' ocean separate regions with efficient and inefficient supply of hydrothermal sourced nutrients—a dividing line for regions of ocean most favourable for life. This would also apply to other ice-covered moons, like Europa, where stratification interfaces could mark the predominant meeting point of hydrothermally derived reductants from below with oxidants delivered from the ice shell above[70,71]. By constraining the extent of stratification in ice-covered oceans, further constraints upon their habitability could be obtained. In particular, improved constraints upon induced mixing within Enceladus' ocean would strongly reduce uncertainty in the transport of hydrothermally -derived tracers to the plumes.

Methods

Model configuration details

Numerical simulations are performed using the Massachusetts Institute of Technology Ocean General Circulation Model (MITgcm;[51]) configured for Enceladus. The MITgcm has been used previously to model the oceans of icy moons[31,47,72] and the ice-covered ocean of Snowball Earth[73–75], which shares similarities with Enceladus' ocean.

The setup is fully non-hydrostatic, so that all components of the Coriolis force are considered—these were previously found to be important for icy moon ocean dynamics[47,72]. The thin shell approximation is relaxed by turning on the MITgcm's deep atmosphere mode. This allows the model to more precisely represent Enceladus' ocean geometry which is of non-negligible thickness relative to its radius. Gravity is allowed to vary with depth in the model, using the formulation of[76]:

$$g(z) = \frac{4\pi G[\rho_{\mathrm{core}}(r_{\mathrm{s}} - H_{\mathrm{i}} - H_{\mathrm{o}})^3 + \rho_{\mathrm{oi}}((r_{\mathrm{s}} - z)^3 - H_{\mathrm{i}} - H_{\mathrm{o}})^3]}{3(r_{\mathrm{s}} - z)^2}, \quad (9)$$

where $G = 6.67 \times 10^{-11}$ m^3 kg^{-1} s^{-2} is the gravitational constant, $\rho_{\mathrm{core}} = 2370$ kg m^{-3} and $\rho_{\mathrm{oi}} = 1000$ kg m^{-3} the approximated mean densities of the core and ocean-ice (combined) layers respectively, $r_{\mathrm{s}} = 252$ km the mean radius at the ice shell surface, z the ocean depth and $H_{\mathrm{i}} = 20$ km and $H_{\mathrm{o}} = 40$ km the mean thickness of the ice and ocean layers respectively[44].

The configuration is 2D, at a 1 degree (~4 km) meridional resolution with 50 layers in the vertical. The vertical resolution coarsens with depth via a hyperbolic tangent profile[77], from ~300 m at the ocean-ice interface, to ~1000 m resolution at the ocean bottom. Finer resolution is used nearer the ice-interface to better resolve shallow stratified layers.

The coarse resolution employed, combined with the lack of a zonal dimension (which provide a necessary reduction in computational cost) means the effects of baroclinic eddies must be parameterised. Here we employ the GMREDI scheme, a flagship standard in Earth ocean modelling. The parameterisation scheme consists of two components: firstly, the Gent-McWilliams (GM) component represents the adiabatic stirring effects of eddies[57], using a bolus (i.e., eddy-induced) velocity [see[78]], parameterised as:

$$\boldsymbol{u}^* = \begin{pmatrix} u^* \\ v^* \\ w^* \end{pmatrix} = \begin{pmatrix} -\partial_z(\kappa_{\mathrm{GM}} S_x) \\ -\partial_z(\kappa_{\mathrm{GM}} S_y) \\ \partial_z(\kappa_{\mathrm{GM}} S_x) + \partial_z(\kappa_{\mathrm{GM}} S_y) \end{pmatrix}, \quad (10)$$

where S is the isoneutral slope (slope of locally referenced potential density) in the x or y directions (denoted by subscript), and κ_{GM} is the isopycnal diffusivity, also referred to as the GM or eddy diffusivity.

Secondly, the Redi component parameterises along-isopycnal mixing induced by mesoscale eddies using a tensor applied to the tracer field, also as a function of the isoneutral slope S[58]. In Earth ocean models, the small slope approximation is typically employed (i.e., $S << 1$). This yields the small slope Redi tensor[79]:

$$K_{\mathrm{redi}} = \begin{Bmatrix} 1 & 0 & S_x \\ 0 & 1 & S_y \\ S_x & S_y & |S|^2 \end{Bmatrix}. \quad (11)$$

We find this assumption to be inappropriate for icy moon oceanography where weak vertical gradients in ocean density can result in slopes orders of magnitude larger than those typically observed in Earth's oceans. Therefore, we employ the full unapproximated Redi tensor[58], defined as:

$$K_{\mathrm{redi}} = \frac{1}{1 + |S|^2} \begin{Bmatrix} 1 + S_y^2 & -S_x S_y & S_x \\ -S_x S_y & 1 + S_x^2 & S_y \\ S_x & S_y & |S|^2 \end{Bmatrix}. \quad (12)$$

A κ_{GM} of 1 m^2 s^{-1} is chosen, found to be near the upper bound of plausible eddy diffusivity values in the eddy resolving 3d simulations of ref. 60. This is chosen as a conservative estimate, given the referenced work did not consider freshwater fluxes from the overlying ice shell as done here, which could further enhance eddy activity. We perform sensitivity tests using lower

values of κ_{GM} as described in the main text (Fig. S4). Due to the near infinite slopes that can develop in statically unstable regions, we apply a slope clipping scheme which limits the magnitude of the GM streamfunction, $\psi_y = \kappa_{GM} S_y$, beyond a slope of 5 to maintain numerical stability. While this introduces diabatic fluxes, it does so only in statically unstable regions which we find has negligible influence upon the penetration depth of a surface stratified layer. We argue this is more robust than the explicit horizontal diffusivity used in previous global simulations of icy moon ocean circulation which introduces (uncontrolled) diabatic fluxes that interfere with the effects of prescribed diapycnal mixing κ_z, rendering sensitivity experiments to mixing impractical.

For reference, numerical solutions for the vertically integrated meridional heat transport achieved by GMREDI are provided in Fig. S5. Heat is transported equatorward, in qualitative agreement with previous work[39,61]. When extrapolated to the full globe, the total meridional heat transport of ~7–10 GW achieved by GMREDI is in approximate agreement with scalings by[61] at $\kappa_z = 10^{-3}$ m^2 s^{-1}. Solutions at lower κ_z produce a larger meridional heat transport than predicted by existing scalings (possibly owing to the diabatic fluxes present within convecting regions, which are more extensive at low κ_z—see Fig. S3). This is not expected to impact the conclusions presented in the main text.

Convection is parameterised using a simple diffusive adjustment scheme, where vertical diffusivity is increased in regions of static instability to represent the vertical mixing of tracers that unresolved convection would have otherwise generated[56]. We set this diffusivity to 1 m^2 s^{-1}, using the scaling of[80], assuming a buoyancy flux induced by our prescribed bottom heat flux (see below). A limitation is that this scheme inhibits slantwise convection (convection parallel to the axes of rotation) and Taylor columns that may be expected to occur on Enceladus[81]. However, given our finding that ocean stratification extent is predominantly controlled by the vertical mixing κ_z and eddy induced mixing κ_{GM} (i.e., processes that can move heat within the stratified region of ocean), we argue this does not affect the robustness of the results and conclusions presented in the main text. Slantwise convection may alter the heat flux at the bottom of the stratified layer nearer the equator, where the rotation axis (and by extension, the direction of slantwise convection) tends towards being perpendicular to the vertical. This could enhance lateral variations in stratification extent. Future work focusing upon accurate representations of convection could determine if this is the case.

Parameters such as ocean depth, rotation rate, planetary radius and surface gravity are set to match those of Enceladus and are given in table S1. We assume a flat ocean bottom and make no attempt to include topography at the upper boundary at this stage, the former owing to lack of constraints[44], and the latter for simplicity.

A geothermal heat flux is applied at the bottom boundary. We borrow the formulation of[31], which yields a bottom heating twice as large at the poles vs the equator, consistent with the tidal heating study of[12]:

$$Q_{core}(\Theta) = \frac{F_{tot}[0.5 Y_{20}(\Theta) + K]}{4\pi K r_c^2}, \tag{13}$$

where $r_c = 192$ km is the core radius (radius to the ocean bottom), $K \approx 0.904$ a constant and Y_{20} a degree 2, order 0 spherical harmonic function (as a function of co-latitude Θ). A total core heat output of F_{tot} = 20 GW is assumed. This is the mean value in the range suggested by[12]. The computed bottom heating profile is shown in Fig. S1 (upper left).

At the upper boundary we apply a fixed freshwater flux to simulate the effects of freezing and melting of an overlying ice shell. We follow the approach of[47], by computing the flow rate of a prescribed ice shell geometry using the ice flow model of[54], then using the ice sheet divergence to compute an implied freezing rate (Fig. S1). We use a sinusiodal curve to represent Enceladus' ice shell geometry in boundary forcing computations, with a mean thickness of 20 km, symmetrical about the equator where thickness is a maximum (10 km thicker than at the poles). While idealised, this captures the broad equator-to-pole variation that has been reconstructed from gravity, libration and shape data[4,44,82] and suffices for our goal here of producing a reasonable approximation for the large-scale variations in freshwater fluxes at the ice-ocean interface. The flow of the ice shell is then computed using the following:

$$M(\phi) = -\frac{2g\frac{\rho_i}{\rho_0}(\rho_0 - \rho_i)H_{ilat}^3}{r_s \eta_{melt} ln^3\left(\frac{T_s}{T_f}\right)} \frac{dH_{ilat}}{d\phi} \int_{T_s}^{T(z)} \int_{T_s}^{T_f} exp\left[\frac{-E_a}{R_g T_f}\left(\frac{T_f}{T_i} - 1\right)\right] ln\left(\frac{T_i'}{T_f}\right) \frac{dT_i'}{T_i'} \frac{dT_i}{T_i}, \tag{14}$$

where g is surface gravity, $\rho_i = 925$ kg m^{-3} and ρ_0 the ice and ocean reference densities respectively. H_{ilat} gives the thickness of the ice layer at a point latitude, r_s the mean radius of Enceladus, η_{melt} the ice melting viscosity (at the base of the ice shell), T_f and T_s the prescribed temperatures at the ice-ocean interface (freezing temperature) and surface respectively. $T_i(z, \phi)$ is the ice temperature (computed using Eq. (S7) from[54]). $E_a = 59.4$ kJ mol^{-1} is the activation energy for diffusion creep, $R_g = 8.31$ J K^{-1} is the gas constant and $T_i' = T_i(z)$ is an integral variable (prime symbol used to distinguish the outer vs inner integral). The surface temperature T_s is computed using a radiative balance at the ice shell surface, given the solar constant at Saturn and assuming a surface bond albedo of 0.81[83], using the analytic approach of[84]. The profile for T_s is shown in Fig. S1 (bottom left).

The implied freezing rate is then computed using the divergence of the ice shell flow:

$$q(\phi) = \frac{1}{r_s \cos\phi} \frac{\partial}{\partial\phi}(M \cos\phi), \tag{15}$$

where ϕ denotes latitude. The freshwater flux profile is given in Fig. S1 (bottom right), for an ice melting viscosity of 10^{-14} Pa s. Freezing is largest at the equator where the prescribed ice geometry is thickest. Melting is largest nearer the poles where ice is thinner. Sensitivity tests, performed at a five times increased η_{melt} (corresponding to a five times stronger ice flow rate) yield similar solutions to that obtained in the main text, but with increased discrepancies relative to the theoretical model at lower κ_{GM} (Fig. S4, right panel).

Temperature at the ocean top is restored to freezing point with a restoring timescale of 30 days. Recent studies have pointed to the importance of meridional temperature gradients at the ice shell[47], particularly in generating baroclinic eddies which may contribute to ocean stratification [see[60]]. We therefore include this effect, by computing the salinity and pressure dependant freezing point implied by the same ice geometry used to compute our freshwater flux, using the formulation of[55]. This yields an ice-interface temperature about 0.1 °C warmer at the poles vs the equator (Fig. S1, middle left). A linear drag coefficient of 10^{-4} m s^{-1} is applied at both the ocean top and ocean bottom. Viscosities are chosen to fix the Prandtl number at 10. Finally, we employ the fully non-linear equation of state of[52] to capture important variations of ocean density (and α_T) with temperature, pressure and salinity.

All simulations are initiated from rest, at a uniform salinity (mean salinity) and reference temperature (freezing temperature assuming ice thickness H_i). Simulations are then run to equilibrium which, dependent on mean salinity and κ_z, takes anywhere between 10000-600000 model years to achieve.

Critical temperature computation and fitting

The following section details methods used to obtain a linear approximation for the critical temperature T_{crit}—the temperature at which the thermal expansion coefficient (α_T) changes sign for a given salinity and pressure.

T_{crit} is first obtained manually, by computing the temperature that coincides with a density maximum, across ranges in ocean salinity and pressures that permit α_T to change sign (0–25 g kg^{-1} and 0–28 MPa respectively). Water density is computed using the non-linear equation of state of ref. 52.

A multiple linear regression is then performed using the SciKit-Learn python package version 1.3.0[85] to obtain coefficients for the linear approximation for the critical temperature:

$$T_{\mathrm{crit}} \approx aS + bP + c, \tag{16}$$

where we find, $a = -0.216$ °C (g kg^{-1})$^{-1}$, $b = -2.11 \times 10^{-7}$ °C Pa^{-1}, and $c = 4.01$ °C (as shown in the main text). Given the dependence of T_{crit} upon pressure is slightly non-linear[86], the regression is performed for pressures relevant to Enceladus, defined here to be 0-7 MPa. The upper bound is the approximate pressure under 60 km of ocean.

The linearly approximated critical temperature for Enceladus as a function of salinity and pressure is shown in Fig. S6 (upper left). The anomaly relative to the manual computation is also shown (Fig. S6, lower left). Mean absolute error relative to the manually computed T_{crit} is ~0.01 °C.

A multiple linear regression is also performed for a range of larger pressures, from 12-28 MPa. The lower bound corresponds to pressures under 10 km ice on Jupiter's moon Europa—an ice-covered, ocean-bearing moon larger than Enceladus, and a target of upcoming missions[87,88]. Mean absolute error is again ~0.01 °C. Coefficients in this case are: $a = -0.221$ °C (g kg^{-1})$^{-1}$, $b = -2.28$ x 10^{-7} °C Pa^{-1}, and $c = 4.23$ °C. The linearly approximated T_{crit} for Europa is shown in Fig. S6 (right).

Critical temperature and freezing temperature comparison

Water freezing temperature, T_{f}, is computed in the 1D theoretical model as a linear function of ocean salinity and pressure at the ice-ocean interface:

$$T_{\mathrm{f}} = -0.055S - 0.753 \times 10^{-7}P + 0.008, \tag{17}$$

obtained by performing a multiple linear regression to the non-linear formulation of ref. 55. In doing so, Eqs. (3) and (17) take identical forms, enabling clarification of the contributions of T_{crit} and T_{f} to the inverse layer thickness (computed with Eq. (5) of the main text). Increasing ocean salinity and ice-interface pressure both act to cool T_{crit} and T_{f}, but the effects of doing so are three–four times stronger for T_{crit}. The constant is negligible in Eq. (17) compared to that in Eq. (3). Overall, this ensures that variations in T_{crit} dominate variations in T_{f} in influencing the inverse layer thickness. Lateral variations in T_{f} (e.g., as induced by variations in ice shell topography) are therefore expected to have little direct effect upon the inverse layer thickness, except where variations in T_{f} prevent α_T from changing sign in parts of the domain.

Application to other icy moons

The theoretical model can be applied to other moons and planets permanently overlain by ice and heated from below. Fig. S7 shows the inversion depth and corresponding age at the ice shell for putative hydrothermally derived tracers within Jupiter's moon Europa. For illustrative purposes, the inversion depth and age are shown for the same ranges in ocean salinity and κ_z as done for Enceladus in the main text. We assume an ice thickness of 10 km[89], and a bottom heat flux of 0.015 W m^{-2}[90], nearer the lower bounds of estimates, to obtain upper bounds on the possible extent of inverse stratification in its ocean. Note that coefficients for the computation of T_{crit} are adjusted slightly as described in the section Critical Temperature Computation and Fitting.

For the assumed ice thickness and bottom heat flux, inverse stratification can only occur if ocean salinity is lower than ~14 g kg^{-1}. Using $H_{\mathrm{strat}} = (T_{\mathrm{crit}*} - T_f)/(-bg\rho_0)$, the maximum possible inverse layer thickness is approximately 8km, regardless of the assumed bottom heating. Even so, the transport timescale through an inverse layer could still exceed 10000 years. This would also apply to materials entering Europa's ocean from above[70], for example oxidants delivered into Europa's ocean via ice shell brines[71]. It has been proposed that delivery of radiolytically derived oxidants from Europa's ice surface into its ocean would improve the availability of redox gradients within Europa's ocean (compared to that in the presence of hydrothermally derived oxidants alone), enhancing its habitability [[91], and references therein]. Yet, if such brines cannot penetrate the stratification, oxidant delivery into Europa's bulk ocean would be slowed. In this case, the extent to which oxidants remain concentrated within the inverse layer would depend upon the efficiency of vertical oxidant transport through the inverse layer, the frequency of brine pulses, and the presence of sink mechanisms at depth.

Data availability

The Data used during analysis and in creating the figures is openly available from the University of Reading Research Data Archive at https://doi.org/10.17864/1947.001320.

Code availability

Code and software, required to reproduce the data used in this manuscript, are openly available from the University of Reading Research Data Archive at https://doi.org/10.17864/1947.001320. The MITgcm is open source and actively maintained at https://github.com/MITgcm/MITgcm/tree/master.

Received: 21 May 2024; Accepted: 15 January 2025;
Published online: 06 February 2025

References

1. Khurana, K. et al. Induced magnetic fields as evidence for subsurface oceans in Europa and Callisto. *Nature* **395**, 777–780 (1998).
2. Iess, L. et al. The tides of Titan. *Science* **337**, 457–459 (2012).
3. Saur, J. et al. The search for a subsurface ocean in Ganymede with Hubble space telescope observations of its auroral ovals. *J. Geophys. Res.: Space Phys.* **120**, 1715–1737 (2015).
4. Thomas, P. et al. Enceladus's measured physical libration requires a global subsurface ocean. *Icarus* **264**, 37–47 (2016).
5. Lainey, V. et al. A recently formed ocean inside Saturn's moon Mimas. *Nature* **626**, 280–282 (2024).
6. Porco, C. et al. Cassini observes the active south pole of Enceladus. *Science* **311**, 1393–1401 (2006).
7. Hedman, M. et al. An observed correlation between plume activity and tidal stresses on Enceladus. *Nature* **500**, 182–184 (2013).
8. Kite, E. S. & Rubin, A. M. Sustained eruptions on Enceladus explained by turbulent dissipation in tiger stripes. *Proc. Natl Acad. Sci.* **113**, 3972–3975 (2016).
9. Choblet, G. et al. Enceladus as a potential oasis for life: Science goals and investigations for future explorations. *Exp. Astronomy* **54**, 809–847 (2022).
10. Hsu, H.-W. et al. Ongoing hydrothermal activities within Enceladus. *Nature* **519**, 207–210 (2015).
11. Waite, J. H. et al. Cassini finds molecular hydrogen in the Enceladus plume: evidence for hydrothermal processes. *Science* **356**, 155–159 (2017).
12. Choblet, G. et al. Powering prolonged hydrothermal activity inside Enceladus. *Nat. Astron.* **1**, 841–847 (2017).
13. Waite, J. H. et al. Liquid water on Enceladus from observations of ammonia and 40ar in the plume. *Nature* **460**, 487–490 (2009).
14. Postberg, F. et al. Detection of phosphates originating from Enceladus ocean. *Nature* **618**, 489–493 (2023).
15. Kotelnikova, S. Microbial production and oxidation of methane in deep subsurface. *Earth-Sci. Rev.* **58**, 367–395 (2002).
16. Kelley, D. S. et al. A serpentinite-hosted ecosystem: the lost city hydrothermal field. *Science* **307**, 1428–1434 (2005).
17. Crane, K., Hecker, B. & Golubev, V. Hydrothermal vents in lake baikal. *Nature* **350**, 281–281 (1991).
18. MacKenzie, S. M. et al. The Enceladus orbilander mission concept: Balancing return and resources in the search for life. *Planet. Sci. J.* **2**, 77 (2021).

19. Fifer, L. M., Catling, D. C. & Toner, J. D. Chemical fractionation modeling of plumes indicates a gas-rich, moderately alkaline Enceladus ocean. *Planet. Sci. J.* **3**, 191 (2022).
20. Schoenfeld, A. M. et al. Particle entrainment and rotating convection in Enceladus ocean. *Commun. Earth Environ.* **4**, 28 (2023).
21. Li, G. et al. Increasing ocean stratification over the past half-century. *Nat. Clim. Change* **10**, 1116–1123 (2020).
22. Iversen, M. H. & Lampitt, R. S. Size does not matter after all: no evidence for a size-sinking relationship for marine snow. *Prog. Oceanogr.* **189**, 102445 (2020).
23. Waite, A., Fisher, A., Thompson, P. A. & Harrison, P. J. Sinking rate versus cell volume relationships illuminate sinking rate control mechanisms in marine diatoms. *Mar. Ecol. Prog. Ser.* **157**, 97–108 (1997).
24. Turner, J. T. Zooplankton fecal pellets, marine snow, phytodetritus and the ocean's biological pump. *Prog. Oceanogr.* **130**, 205–248 (2015).
25. Nishioka, J., Obata, H. & Tsumune, D. Evidence of an extensive spread of hydrothermal dissolved iron in the Indian ocean. *Earth Planet. Sci. Lett.* **361**, 26–33 (2013).
26. Measures, C., Hatta, M., Fitzsimmons, J. & Morton, P. Dissolved al in the zonal n Atlantic section of the us geotraces 2010/2011 cruises and the importance of hydrothermal inputs. *Deep Sea Res. Part II: Topical Stud. Oceanogr.* **116**, 176–186 (2015).
27. Saito, M. A. et al. Slow-spreading submarine ridges in the south Atlantic as a significant oceanic iron source. *Nat. Geosci.* **6**, 775–779 (2013).
28. Resing, J. A. et al. Basin-scale transport of hydrothermal dissolved metals across the South Pacific Ocean. *Nature* **523**, 200–203 (2015).
29. Roshan, S., DeVries, T., Wu, J., John, S. & Weber, T. Reversible scavenging traps hydrothermal iron in the deep ocean. *Earth Planet. Sci. Lett.* **542**, 116297 (2020).
30. Postberg, F. et al. Sodium salts in e-ring ice grains from an ocean below the surface of Enceladus. *Nature* **459**, 1098–1101 (2009).
31. Zeng, Y. & Jansen, M. F. Ocean circulation on Enceladus with a high- versus low-salinity ocean. *Planet. Sci. J.* **2**, 151 (2021).
32. Forel, F. A. *Le Léman: Monographie Limnologique*, vol. 1 (F. Rouge, 1892).
33. Woolway, R. I. et al. Winter inverse lake stratification under historic and future climate change. *Limnol. Oceanogr. Lett.* **7**, 302–311 (2022).
34. Melosh, H., Ekholm, A., Showman, A. & Lorenz, R. The temperature of Europa's subsurface water ocean. *Icarus* **168**, 498–502 (2004).
35. Roquet, F., Ferreira, D., Caneill, R., Schlesinger, D. & Madec, G. Unique thermal expansion properties of water key to the formation of sea ice on earth. *Sci. Adv.* **8**, eabq0793 (2022).
36. Jansen, M. F., Kang, W., Kite, E. S. & Zeng, Y. Energetic constraints on ocean circulations of icy ocean worlds. *Planet. Sci. J.* **4**, 117 (2023).
37. Bire, S. et al. Divergent behavior of hydrothermal plumes in fresh versus salty icy ocean worlds. *J. Geophys. Res.: Planets* **128**, e2023JE007740 (2023).
38. Kang, W., Marshall, J., Mittal, T. & Bire, S. Ocean dynamics and tracer transport over the south pole geysers of Enceladus. *Mon. Not. R. Astron. Soc.* **517**, 3485–3494 (2022).
39. Zeng, Y. & Jansen, M. F. The effect of salinity on ocean circulation and ice–ocean interaction on Enceladus. *Planet. Sci. J.* **5**, 13 (2024).
40. Hay, H. C. & Matsuyama, I. Nonlinear tidal dissipation in the subsurface oceans of Enceladus and other icy satellites. *Icarus* **319**, 68–85 (2019).
41. Wilson, A. & Kerswell, R. R. Can libration maintain Enceladus's ocean? *Earth Planet. Sci. Lett.* **500**, 41–46 (2018).
42. Zhu, P., Manucharyan, G. E., Thompson, A. F., Goodman, J. C. & Vance, S. D. The influence of meridional ice transport on Europa's ocean stratification and heat content. *Geophys. Res. Lett.* **44**, 5969–5977 (2017).
43. Kang, W. The modulation effect of ice thickness variations on convection in icy ocean worlds. *Mon. Not. R. Astron. Soc.* **525**, 5251–5261 (2023).
44. Hemingway, D. J. & Mittal, T. Enceladus's ice shell structure as a window on internal heat production. *Icarus* **332**, 111–131 (2019).
45. Čadek, O., Běhounková, M., Tobie, G. & Choblet, G. Viscoelastic relaxation of Enceladus's ice shell. *Icarus* **291**, 31–35 (2017).
46. Lobo, A. H., Thompson, A. F., Vance, S. D. & Tharimena, S. A pole-to-equator ocean overturning circulation on Enceladus. *Nat. Geosci.* **14**, 185–189 (2021).
47. Kang, W., Mittal, T., Bire, S., Campin, J.-M. & Marshall, J. How does salinity shape ocean circulation and ice geometry on Enceladus and other icy satellites? *Sci. Adv.* **8**, eabm4665 (2022).
48. Wunsch, C. & Ferrari, R. Vertical mixing, energy, and the general circulation of the oceans. *Annu. Rev. Fluid Mech.* **36**, 281–314 (2004).
49. Simmons, H. L., Jayne, S. R., Laurent, L. C. S. & Weaver, A. J. Tidally driven mixing in a numerical model of the ocean general circulation. *Ocean Model.* **6**, 245–263 (2004).
50. Rekier, J., Trinh, A., Triana, S. A. & Dehant, V. Internal energy dissipation in Enceladus's subsurface ocean from tides and libration and the role of inertial waves. *J. Geophys. Res.: Planets* **124**, 2198–2212 (2019).
51. Marshall, J., Hill, C., Perelman, L. & Adcroft, A. Hydrostatic, quasi-hydrostatic, and nonhydrostatic ocean modeling. *J. Geophys. Res.: Oceans* **102**, 5733–5752 (1997).
52. Jackett, D. R. & McDougall, T. J. Minimal adjustment of hydrographic profiles to achieve static stability. *J. Atmos. Ocean. Technol.* **12**, 381–389 (1995).
53. Čadek, O. et al. Long-term stability of Enceladus' uneven ice shell. *Icarus* **319**, 476–484 (2019).
54. Kang, W. & Flierl, G. Spontaneous formation of geysers at only one pole on Enceladus's ice shell. *Proc. Natl Acad. Sci.* **117**, 14764–14768 (2020).
55. Losch, M. Modeling ice shelf cavities in AZ coordinate ocean general circulation model. *J. Geophys. Res.: Oceans* **113** (2008).
56. Klinger, B. A., Marshall, J. & Send, U. Representation of convective plumes by vertical adjustment. *J. Geophys. Res.: Oceans* **101**, 18175–18182 (1996).
57. Gent, P. R. & McWilliams, J. C. Isopycnal mixing in ocean circulation models. *J. Phys. Oceanogr.* **20**, 150–155 (1990).
58. Redi, M. H. Oceanic isopycnal mixing by coordinate rotation. *J. Phys. Oceanogr.* **12**, 1154–1158 (1982).
59. England, M. H. The age of water and ventilation timescales in a global ocean model. *J. Phys. Oceanogr.* **25**, 2756–2777 (1995).
60. Zhang, Y., Kang, W. & Marshall, J. Ocean weather systems on icy moons, with application to Enceladus. *Sci. Adv.* **10**, eadn6857 (2024).
61. Kang, W. Different ice-shell geometries on Europa and Enceladus due to their different sizes: Impacts of ocean heat transport. *Astrophys. J.* **934**, 116 (2022).
62. Zeng, Y., Lobo, A., Miller, S., Starr, B. & Jansen, M. The effect of gas bubbles on nanoparticle transport and ocean circulation on Enceladus. In: *AGU Fall Meeting Abstracts* Vol. 2022, P35D–1908 (2022).
63. Robinson, K. J., Hartnett, H. E., Gould, I. R. & Shock, E. L. Ethene-ethanol ratios as potential indicators of hydrothermal activity at Enceladus, europa, and other icy ocean worlds. *Icarus* **406**, 115765 (2023).
64. Howell, S. et al. Enceladus: An enthalpic jet propulsion laboratory. In: *AGU Fall Meeting Abstracts* Vol. 2023, P43E–3321 (2023).
65. Roberts, J. H. & Nimmo, F. Tidal heating and the long-term stability of a subsurface ocean on Enceladus. *Icarus* **194**, 675–689 (2008).
66. Travis, B. & Schubert, G. Keeping Enceladus warm. *Icarus* **250**, 32–42 (2015).
67. Roberts, J. H. The fluffy core of Enceladus. *Icarus* **258**, 54–66 (2015).

68. Soderlund, K. M. Ocean dynamics of outer solar system satellites. *Geophys. Res. Lett.* **46**, 8700–8710 (2019).
69. Hartmann, R., Stevens, R. J., Lohse, D. & Verzicco, R. Toward understanding polar heat transport enhancement in subglacial oceans on icy moons. *Geophys. Res. Lett.* **51**, e2023GL105401 (2024).
70. Carnahan, E., Vance, S. D., Cox, R. & Hesse, M. A. Surface-to-ocean exchange by the sinking of impact generated melt chambers on Europa. *Geophys. Res. Lett.* **49**, e2022GL100287 (2022).
71. Hesse, M. A., Jordan, J. S., Vance, S. D. & Oza, A. V. Downward oxidant transport through Europa's ice shell by density-driven brine percolation. *Geophys. Res. Lett.* **49**, e2021GL095416 (2022).
72. Ashkenazy, Y. & Tziperman, E. Dynamic Europa ocean shows transient Taylor columns and convection driven by ice melting and salinity. *Nat. Commun.* **12**, 1–12 (2021).
73. Ferreira, D., Marshall, J. & Rose, B. Climate determinism revisited: multiple equilibria in a complex climate model. *J. Clim.* **24**, 992–1012 (2011).
74. Ashkenazy, Y., Gildor, H., Losch, M. & Tziperman, E. Ocean circulation under globally glaciated snowball earth conditions: Steady-state solutions. *J. Phys. Oceanogr.* **44**, 24–43 (2014).
75. Jansen, M. F. The turbulent circulation of a snowball earth ocean. *J. Phys. Oceanogr.* **46**, 1917–1933 (2016).
76. Kang, W. & Jansen, M. On icy ocean worlds, size controls ice shell geometry. *Astrophys. J.* **935**, 103 (2022).
77. Stewart, K. et al. Vertical resolution of baroclinic modes in global ocean models. *Ocean Model.* **113**, 50–65 (2017).
78. Griffies, S. M. The gent–mcwilliams skew flux. *J. Phys. Oceanogr.* **28**, 831–841 (1998).
79. Griffies, S. M. et al. Isoneutral diffusion in a z-coordinate ocean model. *J. Phys. Oceanogr.* **28**, 805–830 (1998).
80. Jones, H. & Marshall, J. Convection with rotation in a neutral ocean: a study of open-ocean deep convection. *J. Phys. Oceanogr.* **23**, 1009–1039 (1993).
81. Goodman, J. Tilted geostrophic convection in icy world oceans caused by the horizontal component of the planetary rotation vector. In: *AGU Fall Meeting Abstracts* Vol. 2012, P51A–2017 (2012).
82. Iess, L. et al. The gravity field and interior structure of Enceladus. *Science* **344**, 78–80 (2014).
83. Spencer, J. et al. Cassini encounters Enceladus: background and the discovery of a south polar hot spot. *Science* **311**, 1401–1405 (2006).
84. Ashkenazy, Y. The surface temperature of europa. *Heliyon* **5**, e01908 (2019).
85. Scikit-learn Developers. LinearRegression (2024). https://scikit-learn.org/stable/modules/generated/sklearn.linear_model.LinearRegression.html.
86. Caldwell, D. R. The maximum density points of pure and saline water. *Deep Sea Res.* **25**, 175–181 (1978).
87. Grasset, O. et al. Jupiter icy moons explorer (juice): An ESA mission to orbit Ganymede and to characterise the Jupiter system. *Planet. Space Sci.* **78**, 1–21 (2013).
88. Howell, S. M. & Pappalardo, R. T. Nasa's Europa clipper—a mission to a potentially habitable ocean world. *Nat. Commun.* **11**, 1–4 (2020).
89. Biersteker, J. B. et al. Revealing the interior structure of icy moons with a Bayesian approach to magnetic induction measurements. *Planet. Sci. J.* **4**, 62 (2023).
90. Howell, S. The likely thickness of Europa's icy shell. *Planet. Sci. J.* **2**, 129 (2021).
91. Hand, K., Sotin, C., Hayes, A. & Coustenis, A. On the habitability and future exploration of ocean worlds. *Space Sci. Rev.* **216**, 1–24 (2020).
92. Crameri, F., Shephard, G. E. & Heron, P. J. The misuse of colour in science communication. *Nat. Commun.* **11**, 5444 (2020).

Acknowledgements

F.A. acknowledges PhD studentship funding from the Science and Technology Facilities Council (STFC) grant ST/W507763/1. Figure 3 uses colour-vision-deficiency-friendly and perceptually uniform colour maps developed by[92] (https://www.fabiocrameri.ch/colourmaps/). We thank W. Kang for providing constructive feedback on the manuscript.

Author contributions

F.A. Derived the theoretical model; developed the numerical model configuration, designed the experiments, performed the numerical simulations, performed the data analysis and interpretation, and wrote the manuscript. D.F. was the lead supervisor of the work. D.F. provided guidance on developing and using the model configuration; contributed ideas and provided guidance on the theory, experiment design and data analysis and interpretation. D.F. provided feedback on, edited, and made additions to the manuscript. A.C. and A.M. were co-supervisors of the work—they contributed ideas and discussion that helped shape the concept for the manuscript. Both provided suggestions and feedback on the manuscript.

Competing interests

The authors declare no competing interests.

Additional information

Supplementary information The online version contains supplementary material available at https://doi.org/10.1038/s43247-025-02036-3.

Correspondence and requests for materials should be addressed to Flynn Ames.

Peer review information *Communications Earth & Environment* thanks Yaoxuan Zeng, Ashley Marie Schoenfeld and the other, anonymous, reviewer(s) for their contribution to the peer review of this work. Primary Handling Editors: João Duarte and Joe Aslin. A peer review file is available